SYNTHETIC BIOLOGY

Combinatorial morphogenetic and mechanical cues to mimic bone development for defect repair

S. Herberg[1]*†, A. M. McDermott[2,3†], P. N. Dang[1], D. S. Alt[1], R. Tang[1], J. H. Dawahare[3], D. Varghai[1], J.-Y. Shin[1], A. McMillan[1], A. D. Dikina[1], F. He[1], Y. B. Lee[1], Y. Cheng[1], K. Umemori[1], P. C. Wong[4], H. Park[1], J. D. Boerckel[2,3,5‡], E. Alsberg[1,6,7‡§]

Endochondral ossification during long bone development and natural fracture healing initiates by mesenchymal cell condensation, directed by local morphogen signals and mechanical cues. Here, we aimed to mimic development for regeneration of large bone defects. We hypothesized that engineered human mesenchymal condensations presenting transforming growth factor–β1 (TGF-β1) and/or bone morphogenetic protein-2 (BMP-2) from encapsulated microparticles promotes endochondral defect regeneration contingent on in vivo mechanical cues. Mesenchymal condensations induced bone formation dependent on morphogen presentation, with BMP-2 + TGF-β1 fully restoring mechanical function. Delayed in vivo ambulatory loading significantly enhanced the bone formation rate in the dual morphogen group. In vitro, BMP-2 or BMP-2 + TGF-β1 initiated robust endochondral lineage commitment. In vivo, however, extensive cartilage formation was evident predominantly in the BMP-2 + TGF-β1 group, enhanced by mechanical loading. Together, this study demonstrates a biomimetic template for recapitulating developmental morphogenic and mechanical cues in vivo for tissue engineering.

INTRODUCTION

Endochondral ossification is an indirect mode of bone formation that occurs during long bone development and natural fracture repair whereby mesenchymal progenitor cells form a cartilage anlage that is replaced by bone (*1*, *2*). In both development and repair, mechanical cues are essential for proper endochondral ossification. For example, experimental fetal paralysis significantly decreases bone mass in ovo (*3*), and motion in utero is important for normal bone and joint development (*4*). Likewise, during fracture repair, the amount and mode of interfragmentary strain determine whether a fracture will heal through endochondral or intramembranous ossification (*3*, *5*–*11*). Although bone fractures heal with 90 to 95% success rates by forming a cartilaginous callus (*12*–*14*), large bone defects greater than 3 cm in length cannot form a callus and exhibit high complication rates, representing a significant clinical burden (*15*). Current standard treatments for large bone defects include autologous bone grafting and delivery of high-dose recombinant human (rh) bone morphogenetic protein-2 (BMP-2) soaked on a collagen sponge carrier; however, these treatments are limited by donor-site morbidity and ectopic bone formation, respectively (*16*, *17*).

Cell-based tissue engineering strategies may provide a promising alternative to bone grafts. One proposed strategy combines osteogenic/progenitor cells with materials that mimic the structural properties of mature bone. However, poor cell engraftment and viability due to insufficient vascular supply limit the efficacy of osteogenic cell delivery (*18*–*21*), and the rigidity of mature bone matrix–like scaffolds can impede stimulatory mechanical loads (*22*). An alternative strategy is to seek to mimic the process by which bone tissue forms during development, namely, endochondral ossification (*23*–*29*). As the cartilage anlage is mechanically compliant, avascular, and capable of naturally recruiting neovasculature and endogenous progenitors and osteoblasts, this approach may overcome key limitations for the regeneration of challenging bone defects. Here, we sought to recapitulate the (i) mesenchymal condensation, (ii) sequential morphogenetic cues, and (iii) mechanical cues that mediate developmental endochondral ossification for regeneration of critical-sized bone defects in adult rats.

Mesenchymal cell condensation and chondrogenic differentiation in the developing limb bud are regulated by sequential morphogenic signals, including transforming growth factor–β (TGF-β) (*30*) and BMP (*31*), which mediate cell condensation and induce the master chondrogenic transcription factors SRY-Box 5 (SOX5), SOX6, and SOX9 (*32*, *33*). Recent studies have shown that avascular cartilage templates derived from human mesenchymal stem cell (hMSC) aggregates are capable of progressing through endochondral ossification (*25*, *26*, *29*, *34*–*37*), producing mineralized matrix, vasculature, and a bone marrow hematopoietic stem cell niche (*38*), but these required extended preculture with exogenous growth factors in vitro for chondrogenic priming. To address this problem, we developed scaffold-free mesenchymal condensations, formed through self-assembly of bone marrow–derived hMSC sheets incorporated with TGF-β1–releasing gelatin microspheres (GM) for in situ chondrogenic priming. These formed robust cartilage tissue in vitro (*39*) and induced endochondral bone defect regeneration after implantation in vivo (*40*). Further, sustained individual or co-delivery of BMP-2 in mesenchymal condensations induced both chondrogenesis and osteogenesis in vitro

[1]Department of Biomedical Engineering, Case Western Reserve University, Cleveland, OH, USA. [2]Department of Orthopaedic Surgery, Perelman School of Medicine, University of Pennsylvania, Philadelphia, PA, USA. [3]Department of Aerospace and Mechanical Engineering, University of Notre Dame, Notre Dame, IN, USA. [4]School of Biomedical Engineering, College of Biomedical Engineering, Taipei Medical University, Taipei, Taiwan. [5]Department of Bioengineering, University of Pennsylvania, Philadelphia, PA, USA. [6]Department of Orthopaedic Surgery, Case Western Reserve University, Cleveland, OH, USA. [7]National Center for Regenerative Medicine, Division of General Medical Sciences, Case Western Reserve University, Cleveland, OH, USA.
*Present address: Departments of Ophthalmology, Cell and Developmental Biology, and Biochemistry and Molecular Biology, SUNY Upstate Medical University, Syracuse, NY, USA.
†These authors contributed equally to this work.
‡Corresponding author. Email: boerckel@pennmedicine.upenn.edu (J.D.B.); ealsberg@uic.edu (E.A.)
§Present address: Departments of Bioengineering and Orthopedics, University of Illinois, Chicago, IL, USA.

(*41*, *42*) and endochondral regeneration of calvarial defects in vivo (*27*). Local morphogen presentation circumvents the need for lengthy exogenous supplementation of inductive signals and enables in vivo implantation of the cellular constructs in a timely and cost-efficient manner, thereby providing a promising system to investigate the progression of mesenchymal condensation through endochondral ossification in vivo.

The mechanical environment considerably influences bone development, homeostasis, and regeneration (*3*, *5*–*11*). To investigate the roles of mechanical cues in large bone defect regeneration, we developed a critical-sized rat femoral bone defect model in which ambulatory load transfer can be controlled by dynamic modulation of axial fixation plate stiffness (*40*, *43*–*45*). We previously showed that load initiation, delayed to week 4 (after the onset of regeneration and bony bridging), significantly enhanced bone formation, biomechanical properties, and local tissue adaptation mediated by BMP-2–releasing hydrogels (*43*–*45*). Recently, we showed that in vivo loading of engineered mesenchymal condensations, containing TGF-β1–releasing gelatin microparticles, restored bone function through endochondral ossification (*40*).

However, these studies focused on single morphogen presentation, and bone development features an intricate and tightly coordinated sequence of both morphogenetic and mechanical cues. Here, we investigated the combinatorial roles of controlled temporal presentation of TGF-β1 and/or BMP-2 to mimic events in the developing limb bud, with in vivo mechanical loading. To control local morphogen presentation, we engineered mesenchymal condensations incorporated with gelatin or mineral microparticles for local release of TGF-β1 to drive chondrogenesis and BMP-2 to promote remodeling of the cartilaginous anlage to bone, respectively. To regulate in vivo mechanical conditions, we used the same custom fixation plates described previously (*40*, *43*–*45*) that modulate fixation plate stiffness through elective unlocking, allowing increased ambulatory load sharing between the defect and fixation plate (see Materials and Methods for stiffness values of the plates). We previously estimated that interfragmentary strains of 2 to 3% exist in the stiff and delayed loading groups at day 0, 5 to 10% in the delayed group after plate unlocking, and 0.5 to 3% in all groups at week 12 (*40*). Variables such as the tissue composition, amount, and growth kinetics temporally regulate the strain state in the defects. We found that morphogen co-delivery and in vivo mechanical loading combinatorially regulated bone regeneration and directed ossification mode, with combined treatment inducing full functional restoration of bone mechanical properties.

RESULTS

Effects of in vivo mechanical loading on autograft-mediated bone regeneration

Previously, we (*40*, *44*, *45*) and others (*46*, *47*) found that in vivo mechanical loading can enhance the regeneration of large bone defects. First, to test whether loading can enhance autograft-mediated bone regeneration, we treated critical-sized (8 mm) defects in Rowett nude (RNU) rat femora with morselized cortical bone autografts in two groups: control (stiff fixation plates) and delayed loading (compliant plates, unlocked to allow ambulatory load transfer at week 4) (fig. S1A). We evaluated bone formation over 12 weeks by longitudinal microcomputed tomography (microCT) imaging. Mechanical loading did not affect autograft-mediated bone formation (fig. S1, B and C). Since stiff load–bearing scaffolds can impede load-induced bone repair (*22*), we next tested whether non–load-bearing mesenchymal condensations containing local presentation of BMP-2 could promote bone defect repair.

Comparison of BMP-2–containing mesenchymal condensations with the current standard of care in the absence of mechanical loading

To this end, we compared the bone formation capacity of BMP-2–containing mesenchymal condensations with either autograft or BMP-2–loaded collagen sponge controls, without mechanical loading (i.e., stiff fixation). Mesenchymal condensations were assembled with mineral-coated hydroxyapatite microparticles (MCM) for in situ controlled presentation of 2 μg of BMP-2 (*27*, *41*, *42*, *48*, *49*). The BMP-2/collagen group received the same dose of BMP-2 (2 μg), adsorbed onto lyophilized collagen sponges, and the autograft group featured morselized cortical bone.

We performed high-resolution ex vivo microCT analysis at week 12 to evaluate bone formation and architecture. Both BMP-2/collagen and morselized autograft produced significantly greater bone volume fraction, trabecular number, and smaller trabecular separation compared to BMP-2–containing mesenchymal condensations (fig. S2, A to C). However, ectopic bone formation (i.e., bone extending beyond the 5-mm defect diameter) was significantly greater in defects treated with BMP-2 delivered on collagen compared to BMP-2–containing mesenchymal condensations (~3-fold) or autografts (~4-fold; fig. S2, B and C). While the development-mimetic mesenchymal condensations induced bone formation with less ectopic bone than BMP-2/collagen, their ultimate regenerative capacity was inferior.

Controlled combinatorial morphogen presentation with in vivo mechanical load transfer

Natural bone development and fracture repair occur through endochondral ossification in response to combined chondrogenic, osteogenic, and mechanical cues. Therefore, we hypothesized that these factors would be required in a combinatorial fashion to induce bone regeneration in a manner that reproduces natural bone formation. To this end, we next treated defects with mesenchymal condensations containing local presentation of TGF-β1 and/or BMP-2, with or without in vivo mechanical loading.

We previously showed that delayed in vivo mechanical loading, initiated at week 4 by compliant fixation plate unlocking, moderately enhanced (18%) bone regeneration by cell-free hydrogel-delivered BMP-2 (*44*, *45*) and substantially enhanced (180%) endochondral regeneration by TGF-β1–incorporated mesenchymal condensations (*40*). Here, we investigated the interactions of mechanical loading with morphogen presentation. TGF-β1 was presented in GM for early release and BMP-2 from MCM for sustained release (*39*). Three morphogen conditions were evaluated: mesenchymal condensations with empty microparticles (empty/control), condensations with BMP-2–releasing microparticles, and condensations with BMP-2 + TGF-β1–releasing microparticles. Each was implanted in vivo with either stiff plates (control) or compliant plates unlocked at week 4 (delayed loading), for a total of six groups (Table 1).

In vivo radiography and microCT analyses

We performed longitudinal x-ray radiography and microCT analyses at weeks 4, 8, and 12. BMP-2–containing mesenchymal condensations

enhanced bone regeneration relative to empty/controls at weeks 8 and 12 with both loading regimens [Fig. 1, A (red lines), B (red boxes), and C]. Some instances of bridging were observed (stiff, 3 of 9; compliant, 4 of 7; fig. S3). The BMP-2–mediated regenerative effects were significantly enhanced by TGF-β1 co-delivery [Fig. 1, A (blue lines), B (blue boxes), and C]. Bridging was achieved in nearly all dual morphogen samples (stiff, 9 of 11; compliant, 9 of 10; fig. S3).

Mechanical loading significantly elevated the bone volume accumulation rate during the 4 weeks immediately after the compliant plate unlocking in BMP-2 + TGF-β1–presenting mesenchymal condensations compared to all other groups and time intervals (Fig. 1B). New bone formation was negligible in empty/control samples, regardless of mechanical loading [Fig. 1, A (black lines), B (white boxes), and C], and none achieved bridging by week 12 (stiff, 0 of 8; compliant, 0 of 4; fig. S3). Thus, transplanted mesenchymal condensations induced bone regeneration dependent on morphogen identity, and mechanical loading influenced the rate of bone formation during the 4 weeks following load initiation in samples containing both BMP-2 and TGF-β1.

Ex vivo microCT analysis

We then evaluated tissue composition and organization at high resolution by ex vivo microCT analysis at week 12. Empty/control mesenchymal condensations without morphogen presentation failed to induce healing regardless of mechanical loading, with new bone formation merely capping the exposed medullary canals, predominantly on the proximal end (Fig. 2 and fig. S4). Both BMP-2 and BMP-2 + TGF-β1 presentation enhanced bone regeneration compared to empty/control mesenchymal condensations (Fig. 2, A and B). New bone within the defects exhibited an approximately uniform proximal-to-distal distribution (fig. S4A) and lacked notable ectopic bone (fig. S4B), in contrast to BMP-2 delivery on collagen sponge (fig. S1). Dual morphogen presentation and mechanical loading together produced regenerated bone with a trabecular internal architecture contained within a cortical shell, quantitatively similar in structure to native trabecular/cortical bone architecture (Fig. 2, C to E, and fig. S4, C to F). These data show that bone distribution and architecture were determined primarily by presented morphogen identity.

Table 1. Experimental design.

Group	Morphogen condition	Mechanical loading condition
1	Empty/control	Stiff
2	BMP-2	Stiff
3	BMP-2 + TGF-β1	Stiff
4	Empty/control	Delayed (compliant plate unlocked at week 4)
5	BMP-2	Delayed (compliant plate unlocked at week 4)
6	BMP-2 + TGF-β1	Delayed (compliant plate unlocked at week 4)

Restoration of mechanical bone function

Next, we evaluated the restoration of limb mechanical properties by torsion testing to failure at week 12, in comparison to age-matched intact femurs. BMP-2 + TGF-β1–containing mesenchymal condensations enhanced stiffness and failure torque compared to empty/controls. Mechanical loading did not significantly alter mechanical properties compared to corresponding stiff plate controls for each group but significantly increased the mean polar moment of inertia (pMOI) (a measure of structural cross-sectional geometry) and fully restored functional mechanical properties in the BMP-2 + TGF-β1 group (Fig. 3, A to C), with statistically equivalent torsional stiffness and maximum torque at failure compared to age-matched intact femurs (Fig. 3, A and B, cf. gray bands).

To identify the key structural predictors of mechanical behavior (*50*), we performed a type II multivariate best subset regression analysis with model predictors selected by minimization of the Akaike's information criterion (AIC) (*51*). For torsional stiffness, bone volume fraction, trabecular separation, and minimum pMOI were the best combined predictors (Fig. 3E and fig. S5, A to D). For maximum torque, bone volume fraction and minimum pMOI were the best combined predictors (Fig. 3F and fig. S5, E to H). Thus, the mechanical properties were determined by the amount, distribution and trabecular organization of the regenerate bone. Together, these data indicate that restoration of biomechanical competence was dependent on the identity of presented morphogens and induced full functional repair only by dual morphogen presentation with in vivo mechanical loading.

In vitro signaling and differentiation analyses

We hypothesized that the cellular organization into condensations and the development-mimetic morphogen presentation would induce endochondral bone formation. TGF-β superfamily ligands bind to type I and II serine/threonine kinase receptor complexes and transduce signals via SMAD proteins (*52*). In the developing limb, TGF-β signaling has been shown to occur early during the chondrogenic cascade, before the BMPs (*30*, *32*, *33*). Further, a recent study proposed that transient activation of the TGF-β pathway may be required to promote a chondrogenic response to BMP signaling during later stages of chondrogenesis (*53*). Therefore, we next tested the effects of combinatorial morphogen presentation on chondrogenic and osteogenic activity of microparticle-containing hMSC sheets used to form the mesenchymal condensations in vitro. As prepared for in vivo transplantation, TGF-β1 was presented in an early manner by release from GM, while BMP-2 was released in a more sustained manner from MCM.

After 2 days in vitro culture (coinciding with the time of in vivo transplantation), the engineered hMSC sheets exhibited homogeneous cellular organization across groups, with uniformly distributed microspheres and no detectable glycosaminoglycan (GAG) or mineral deposition (Fig. 4A and fig. S6A). Transcript analysis of key differentiation markers revealed that either TGF-β1 or BMP-2 presentation alone significantly induced mRNA expression of genes indicative of both chondrogenic [SOX9, aggrecan (ACAN), and collagen type 2A1 (COL2A1)] and osteogenic [alkaline phosphatase (ALP)] priming, relative to growth factor–free controls (Fig. 4B and fig. S6B). BMP-2 + TGF-β1 co-delivery further increased the expression of SOX9, ACAN, COL2A1, ALP, and osterix mRNA (Fig. 4B). Last, BMP-2 presentation significantly increased both SMAD3 and SMAD5 phosphorylation relative to empty controls without

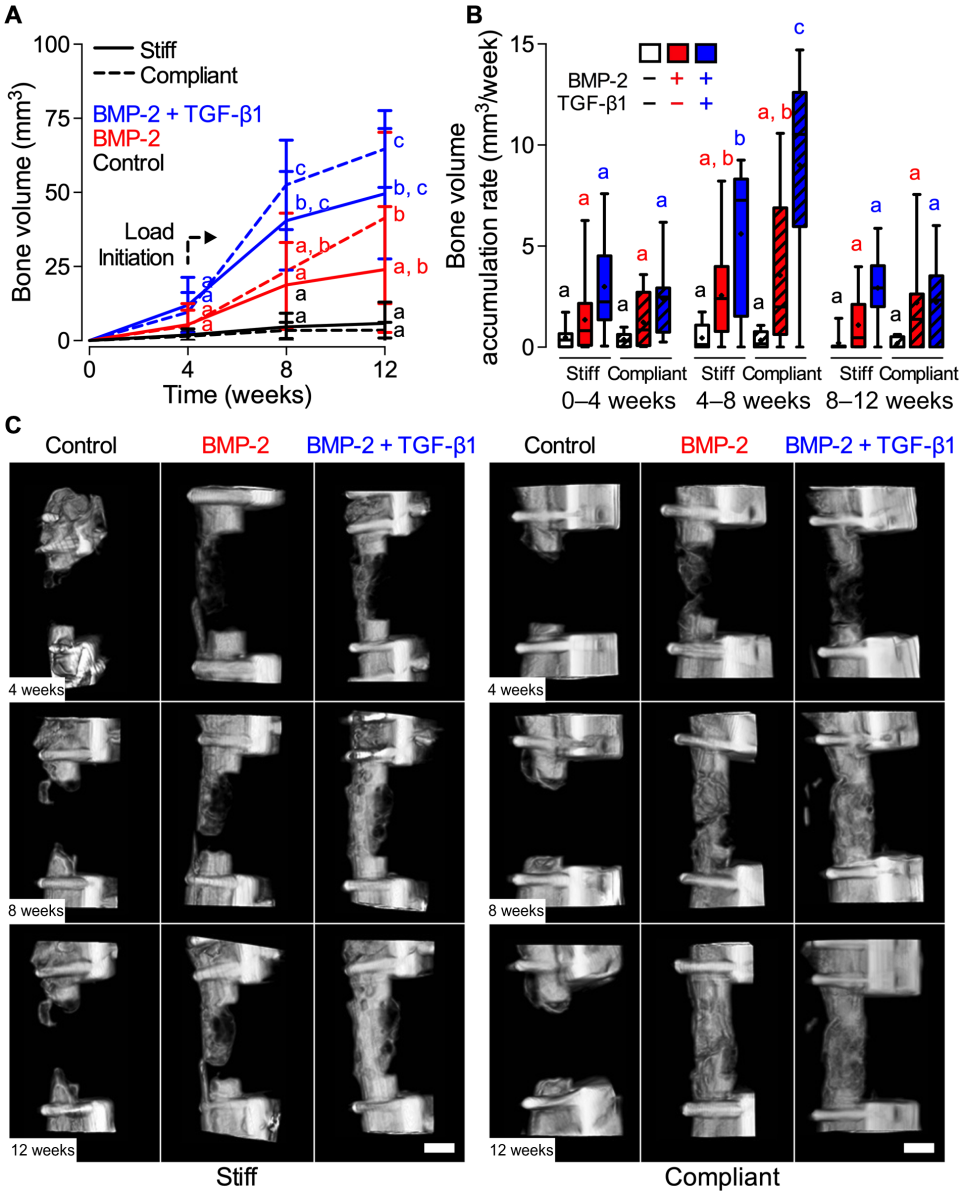

Fig. 1. Effects of morphogen priming of engineered mesenchymal condensations and in vivo mechanical loading on longitudinal bone formation and bone accumulation rate. (**A**) Longitudinal quantification of bone volume at weeks 4, 8, and 12 by in vivo microCT ($n = 4$ to 11 per group). Data are shown as means ± SD. (**B**) Bone volume accumulation rate, defined as bone volume accrual over each 4-week interval. Box plots display median as horizontal line, mean as +, interquartile range as boxes, and minimum/maximum range as whiskers. (**C**) Representative three-dimensional (3D) microCT reconstructions showing bone formation per group over time. Representative samples were selected on the basis of mean bone volume at week 12. Scale bars, 3 mm. Comparisons between groups were evaluated by two-way repeated measures analysis of variance (ANOVA) with Tukey's post hoc tests. Repeated significance indicator letters (a, b, and c) signify $P > 0.05$, while groups with distinct indicators signify $P < 0.05$ at each time point. Comparisons between time points were not assessed.

growth factor and was significantly potentiated by TGF-β1 co-delivery (Fig. 4, C and D). These in vitro data suggest that presentation of either BMP-2 or BMP-2 + TGF-β1 induced chondrogenic lineage priming via both SMAD3 and SMAD5 signaling at the time of implantation.

In vivo tissue differentiation and composition

Next, to test the combinatorial effects of morphogen presentation and mechanical loading on local tissue differentiation, endochondral lineage progression, and matrix organization in vivo, we performed histological analyses of defect tissues at weeks 4 and 12. Empty/control mesenchymal condensations exhibited predominantly fibrous and adipose tissue spanning the defects, and bone formation only capping the diaphyseal ends was apparent (Fig. 5, A and B, and figs. S7 and S8, A, D, G, and J). BMP-2–containing mesenchymal condensations induced the formation of primary woven bone and lamellar bone with lacunae-embedded osteocytes surrounded by marrow-like tissue by week 4 and increased lamellar bone by week 12 (Fig. 5A). Aside from stiff control at 4 weeks, empty/control and BMP-2–containing groups exhibited minimal Safranin-O–stained GAG matrix

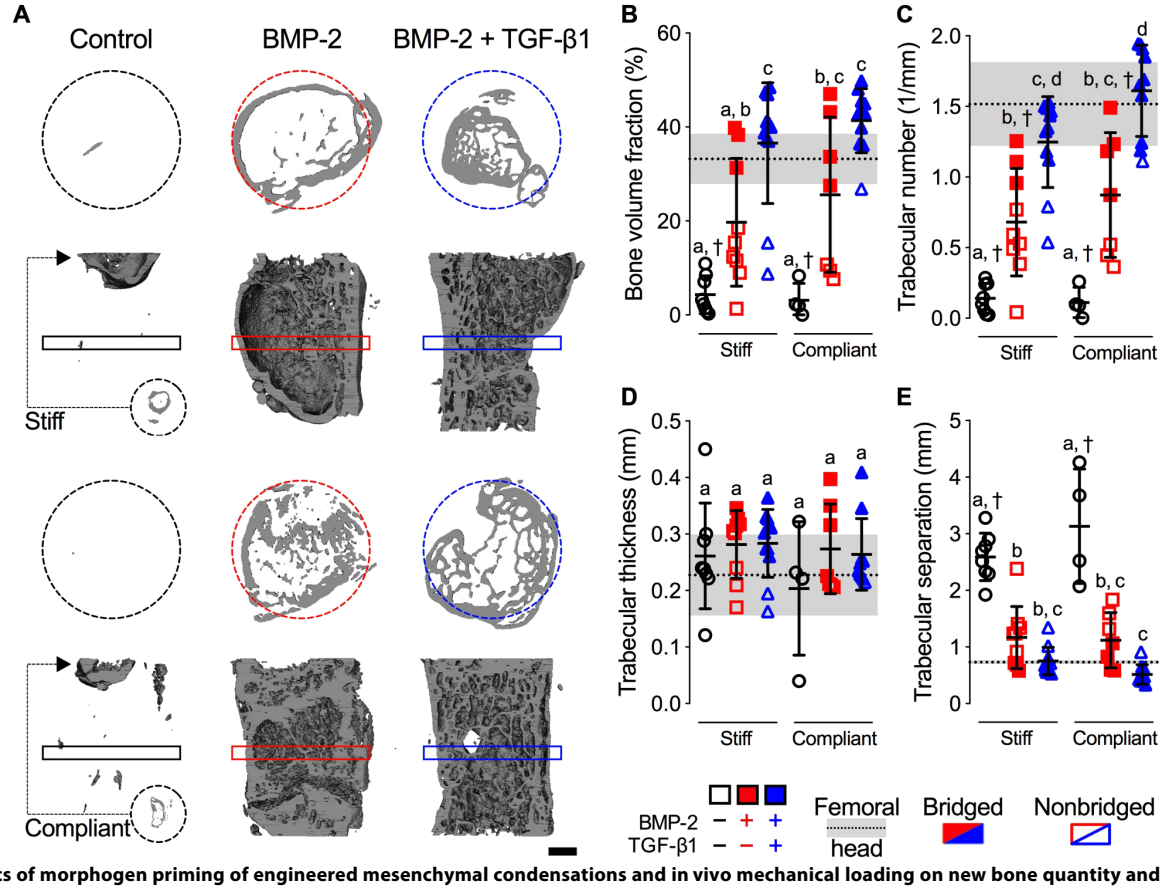

Fig. 2. Effects of morphogen priming of engineered mesenchymal condensations and in vivo mechanical loading on new bone quantity and architecture. (**A**) Representative 3D microCT reconstructions, with bone formation illustrated at mid-shaft transverse (top) and sagittal (bottom) sections at week 12, selected on the basis of mean bone volume. Dashed circles show 5-mm defect region. Rectangular boxes illustrate transverse cutting planes. Note that, due to minimal bone regeneration, additional transverse sections for stiff and compliant no growth factor controls were derived from the proximal end of the defect (small dashed circles and arrows). Scale bar, 1 mm. (**B**) Morphometric analysis of bone volume fraction, (**C**) trabecular number, (**D**) trabecular thickness, and (**E**) trabecular separation at week 12 ($n = 4$ to 11 per group), shown with corresponding measured parameters of femoral head trabecular bone ($n = 3$; dotted lines with gray shading: means ± SD; †$P < 0.05$ versus femoral head). Individual data points are shown as means ± SD. Comparisons between groups were evaluated by two-way ANOVA with Tukey's post hoc tests. Repeated significance indicator letters (a, b, and c) signify $P > 0.05$, while groups with distinct indicators signify $P < 0.05$.

at both time points (Fig. 5, A and B, and figs. S7 and S8, B, E, H, and K). Co-delivery of BMP-2 + TGF-β1 induced robust bone formation exhibiting lacunae-embedded osteocytes in well-defined trabeculae with peripheral-positive GAG staining, evidence of prior cartilaginous template transformation. Mechanical loading of BMP-2 + TGF-β1–containing mesenchymal condensations promoted formation of growth plate–like, transverse cartilage bands that featured zonal organization of mature and hypertrophic chondrocytes with prominent Safranin-O–stained GAG matrix embedded in trabecular bone and aligned orthogonal to the principal ambulatory load axis (Fig. 5, A and B and figs. S7 and S8, C, F, I, and L). Hypertrophic chondrocytes and new bone formation at the interface were indicative of active endochondral bone formation in the dual morphogen group with mechanical loading at both 4 and 12 weeks (Fig. 5B).

Together, these data suggest that, although both BMP-2 and BMP-2 + TGF-β1 induced chondrogenic priming before implantation, endochondral ossification in vivo was most strongly apparent with morphogen copresentation. Further, in vivo mechanical cues potentiated cartilage formation and prolonged endochondral ossification.

DISCUSSION

The aim of this study was to replicate the cellular, biochemical, and mechanical environment present during limb development for functional regeneration of large segmental bone defects. Specifically, we used (i) engineered mesenchymal condensations formed by cellular self-assembly, which contained (ii) microparticle-mediated growth factor presentation to activate specific morphogenetic pathways in situ and which, upon implantation, were exposed to (iii) in vivo mechanical loading. We tested the hypothesis that TGF-β1 and/or BMP-2 presentation from encapsulated microparticles within engineered mesenchymal condensations would promote endochondral regeneration of critical-sized femoral defects in a manner dependent on the in vivo mechanical environment. While both BMP-2 and BMP-2 + TGF-β1 presentation induced chondrogenic priming at the time of in vivo transplantation, endochondral ossification was most strongly evident in the dual morphogen group and was enhanced by mechanical loading. Specifically, in vivo ambulatory mechanical loading significantly enhanced the rate of bone formation in the 4 weeks after load initiation in the dual morphogen group, improved bone distribution in the callus, and fully restored mechanical bone function. In contrast, mechanical loading had no effect on bone regeneration

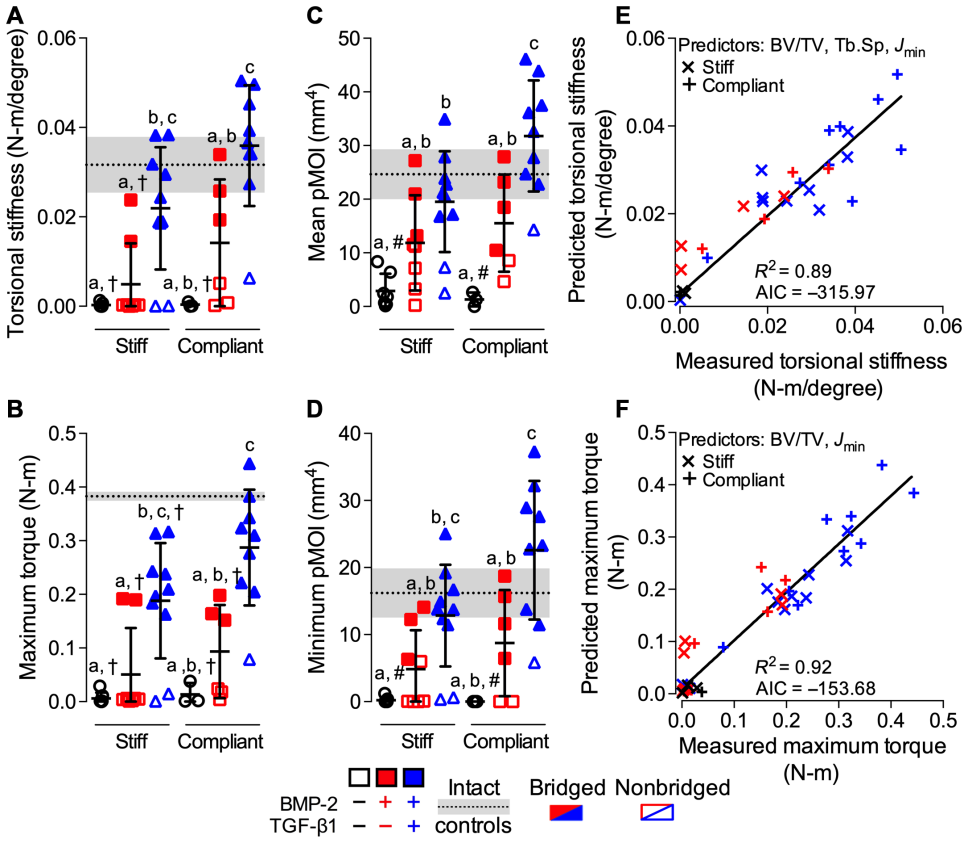

Fig. 3. Effects of morphogen priming of engineered mesenchymal condensations and in vivo mechanical loading on functional defect regeneration. (**A**) Torsional stiffness, (**B**) maximum torque at failure, (**C**) mean pMOI, and (**D**) minimum pMOI. Best subset regression analysis (R^2) with lowest Akaike's information criterion (AIC) value for measured and predicted (**E**) torsional stiffness and (**F**) maximum torque at failure indicating significant contributions of bone volume fraction (BV/TV), trabecular separation (Tb.Sp), and minimum pMOI (J_{min}). Individual data points are shown as means ± SD ($n = 3$ to 10 per group). Comparisons between groups were evaluated by two-way ANOVA with Tukey's post hoc tests. Repeated significance indicator letters (a, b, and c) signify $P > 0.05$, while groups with distinct indicators signify $P < 0.05$. Biomechanical and structural parameters are shown with age-matched intact bone properties, with pMOI obtained from the same mid-shaft region of interest (ROI) as used for the defects ($n = 3$; dotted lines with gray shading: means ± SD; †$P < 0.05$ and #$P < 0.05$ versus intact bone).

in empty/control mesenchymal condensations without morphogen presentation and likewise had no effect on autograft-mediated repair.

Multiple reports have described self-assembled hMSC aggregates to form cartilage templates that can undergo hypertrophy and progress through endochondral ossification in vivo (*25*, *26*, *29*, *34*–*37*). In these studies, chondrogenic priming was achieved by means of exogenously supplied morphogens, involving in vitro preculture of 3 weeks and longer (*25*, *26*, *29*, *34*–*37*). This requires time and associated costs and limits the precision of morphogen spatial distribution control. Further, few studies to date have achieved function-restoring bone formation in orthotopic models using this strategy (*28*, *29*, *54*). We previously demonstrated that sequential in situ morphogen presentation to mesenchymal condensations, using MCM (*49*) and cross-linked GM (*39*) to control the bioavailability of BMP-2 and TGF-β1, respectively, facilitates both chondrogenic and osteogenic differentiation in vitro (*41*) and promotes calvarial bone regeneration via endochondral ossification in vivo (*27*). We also found in mesenchymal condensations with local TGF-β1 presentation that devitalization of the cells after condensation assembly but before transplantation abrogated bone formation, suggesting that both the presented morphogens and cells are important for the endochondral bone formation response (*40*). Here, we show that this spatiotemporally controllable and localized morphogen delivery strategy, inspired by early limb development, eliminates the need for time- and cost-ineffective predifferentiation of the cellular constructs and achieved mechanically functional regeneration without the ectopic bone formation associated with BMP-2/collagen.

In addition to their efficacy in morphogen presentation, the mesenchymal condensations facilitated endochondral healing by providing a nonstructural, immature intermediate, much like a callus in fracture healing or cartilage anlage in limb development. We showed previously that structural scaffolds that mimic the material properties of mature bone shield tissue from the stimulatory and beneficial effects of mechanical load during healing (*22*), suggesting that having a flexible intermediate structure is a more suitable graft material for mechanical regulation of bone regeneration. Here, we found that in vivo mechanical loading via compliant fixation exerted stimulatory effects on defect healing, particularly in the period of plate actuation (4 to 8 weeks), which resulted in complete functional bone regeneration (i.e., restoration of biomechanical competency comparable to unoperated, intact limbs). These data indicate the importance of morphogen presentation for stem cell–mediated regeneration of bone defects and potentially imply that the high stiffness of autograft bone may interfere with load-induced bone formation.

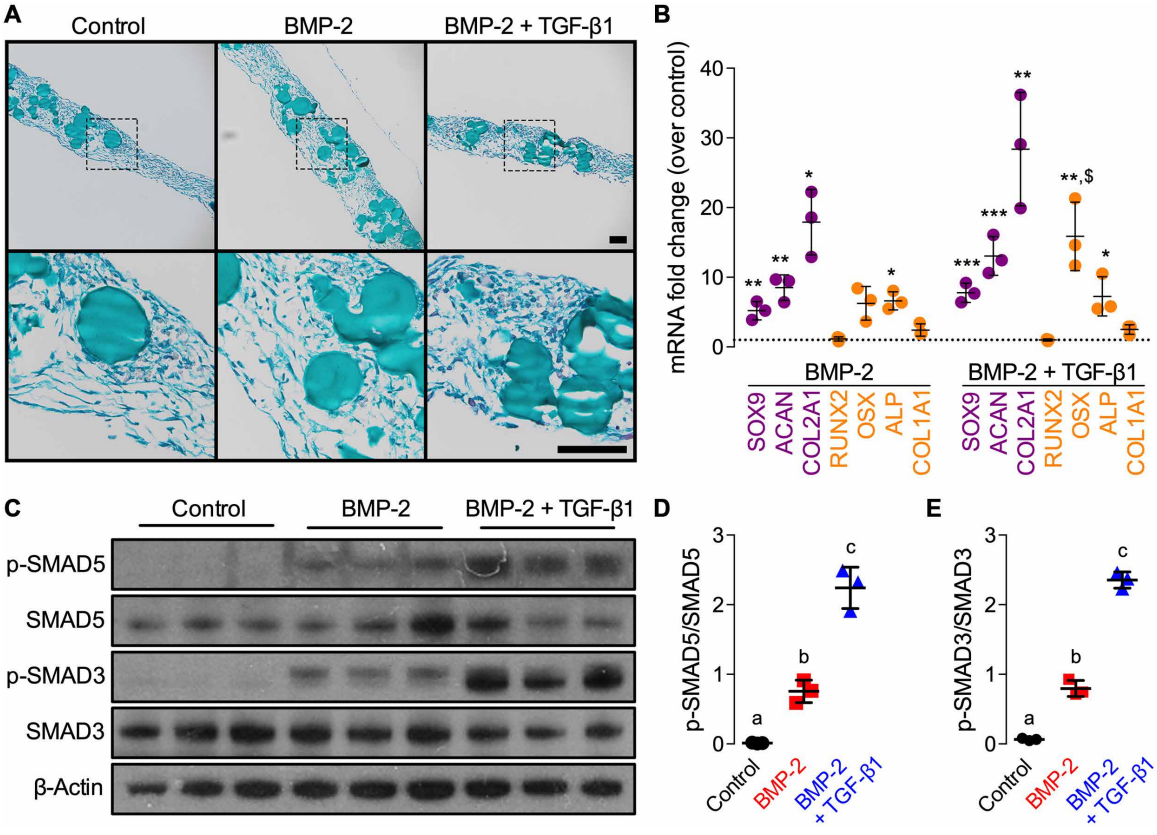

Fig. 4. Effects of morphogen priming of engineered mesenchymal condensations on in vitro chondrogenic lineage specification at the time of implantation. Histological Safranin-O/Fast green staining of representative microparticle-containing hMSC sheets at the time of implantation (2 days; $n = 3$ per group). Scale bars, 100 μm (top, x10; bottom, x40 magnification of dotted squares). (**B**) Normalized mRNA fold change over control of key chondrogenic or osteogenic markers by quantitative reverse transcription polymerase chain reaction (qRT-PCR; $n = 3$ per group; $^*P < 0.05$, $^{**}P < 0.01$, $^{***}P < 0.001$ versus empty/control; $\$P < 0.05$ versus BMP-2–containing hMSC sheets). (**C**) Representative immunoblots and (**D**) relative quantification of phosphorylated SMAD5 (p-SMAD5)/SMAD5 and (**E**) p-SMAD3/SMAD3 in lysates of day 2 hMSC sheets ($n = 3$ per group). β-Actin served as the loading control. Individual data points are shown as means ± SD. Comparisons between groups were evaluated by one-way ANOVA with Tukey's post hoc tests. Repeated significance indicator letters (a, b, and c) signify $P > 0.05$, while groups with distinct indicators signify $P < 0.05$.

Compressive interfragmentary motion is necessary for cartilaginous callus formation and endochondral ossification during fracture healing (*9*, *55*), and here, the presence of growth plate–like cartilage structures, exhibiting zonal organization of mature and hypertrophic chondrocytes embedded in marrow-containing trabecular bone, suggests that BMP-2 + TGF-β1–containing mesenchymal condensations facilitated defect healing chiefly through endochondral ossification. This was consistent with a recent study, demonstrating that a chondrogenic response to BMP-4 is dependent on transient activation of TGF-β signaling in the early limb bud (*53*). In vitro analysis confirmed robust chondrogenic priming of the cellular constructs at the time of surgery. While this was also the case with BMP-2 only–presenting mesenchymal condensations, upon defect implantation these constructs stimulated overall inferior bone regeneration compared to dual morphogen groups independent of the in vivo mechanical environment. Nevertheless, no ectopic bone formation, as seen with BMP-2 soaked on collagen at ~2 μg (*56*), was observed, similar to autografts as the other clinical standard we initially tested our technology against. This suggests an improved safety profile in the context of BMP-2 delivery from scaffold-free, self-assembled cellular constructs. The mechanical environment also influences neovascularization during endochondral ossification, and we recently showed that mechanical forces regulate angiogenesis and vascular remodeling during endochondral regeneration of large bone defects by TGF-β–containing mesenchymal condensations (*40*). Future studies will explore the interactions of morphogen identity and presentation with mechanical cues for large bone defect regeneration.

In conclusion, this study presents a human progenitor cell–based bone tissue engineering approach that recapitulates certain aspects of the normal endochondral cascade in early limb development. Implantation of chondrogenically primed high-density mesenchymal condensations, achieved through in situ morphogen presentation rather than lengthy preculture, in large bone defects that would otherwise not heal if left untreated reestablished biomechanical competency in limbs stabilized with custom compliant fixation plates with elective actuation at 4 weeks, after stable fixation to initiate bone regeneration.

Further studies may elucidate the role of elective actuation timing in this regenerative strategy. Here, all mechanically loaded plates were unlocked at 4 weeks regardless of growth factor treatment. However, this does not take into account the combination of tissues in each defect that were shown to differ with growth factor treatment and may affect their different responses to mechanical load. Although challenging for this particular animal model, future studies could assess more radiographic time points to determine the most appropriate point of unlocking for each group or animal. This would in

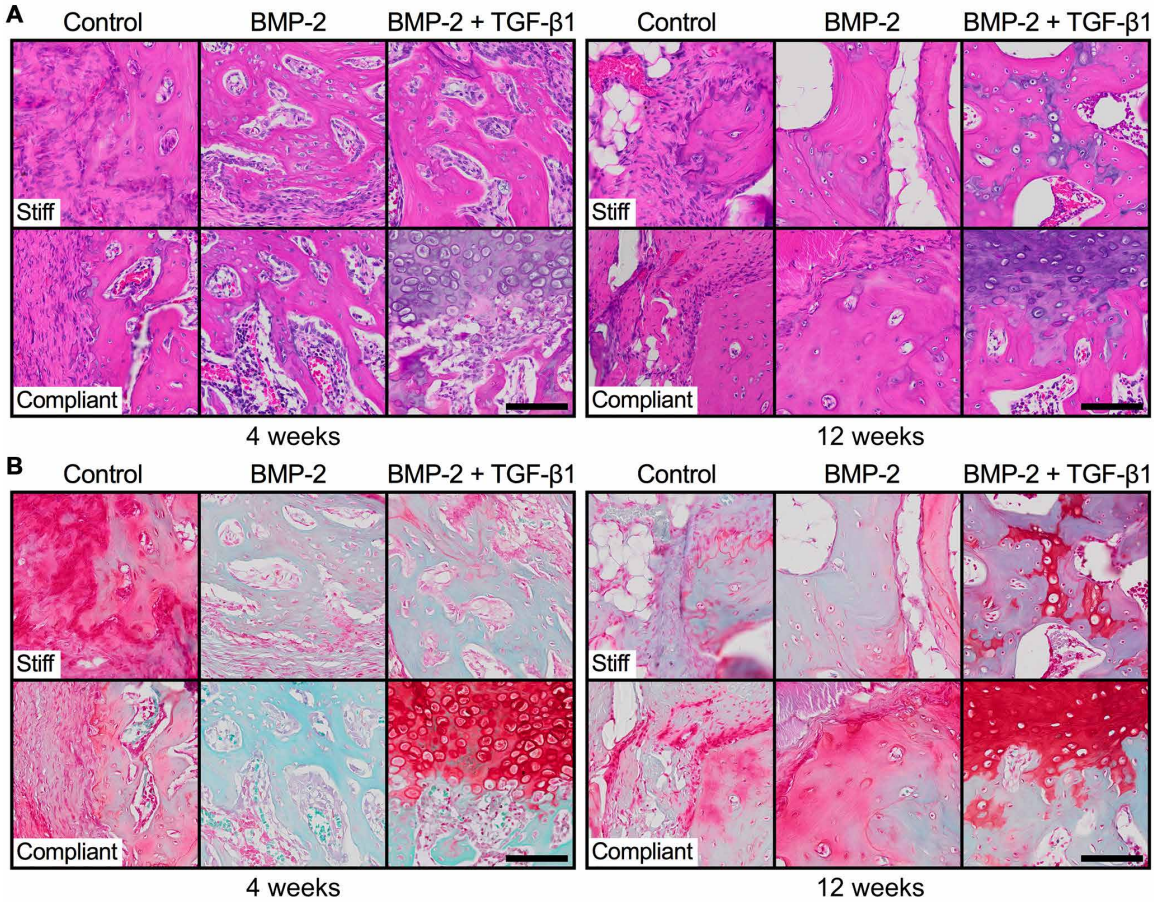

Fig. 5. Effects of morphogen priming of engineered mesenchymal condensations and in vivo mechanical loading on tissue-level bone regeneration. Representative histological (**A**) hematoxylin and eosin and (**B**) Safranin-O/Fast green staining of defect tissue at week 4 (left) and week 12 (right), with stiff (top) and compliant fixation (bottom), selected on the basis of mean bone volume. Scale bars, 100 μm (×40).

fact be more akin to clinical bone repair approaches in which sufficient tissue growth is observed before stresses can be applied to the affected bone. Alternatively, in this model, the maturity of the mesenchymal condensation could be modulated before implantation to understand how the cell state at the time of implantation influences the endochondral response to mechanical load. Our findings are of clinical relevance and advance the current understanding in the growing field of developmental engineering. Furthermore, the system described herein can be used to study the complex biophysical mechanisms that govern tissue regeneration in health and disease.

MATERIALS AND METHODS

Study design

The objective of this work was to mimic the cellular, biochemical, and mechanical environment of the endochondral ossification process during early limb development via in situ morphogen priming of high-density mesenchymal condensations and controlled in vivo mechanical cues upon implantation in large bone defects. We used the established critical-sized rat femoral segmental defect model in 12-week-old male RNU rats with custom internal fixation plates that allow controlled transfer of ambulatory loads in vivo. The sample size was determined with G*Power software (*57*) based on a power analysis using population SDs and estimated effect sizes from our prior studies (*40*, *45*). The power analysis assumed a two-tailed α of 0.05, power of 0.8, and effect sizes of ranging from 0.1 to 0.3. A minimum sample number of $n = 6$ per group was computed, with an ideal sample number of $n = 12$ for all nondestructive and destructive analyses per time point. An $n = 10$ was selected for all nondestructive and destructive analyses per time point, accommodating a 5 to 10% complication rate consistent with our prior studies. Animals were randomly assigned to the treatment groups for both studies. Where indicated, limbs were excluded from the analysis based on radiographic evidence of fixation plate failure. Data collection occurred at predetermined time points informed by previous studies. All analyses were performed by examiners blinded to the treatment group.

Experiments and study groups

Initial studies

For the first initial study, the experimental design featured one treatment group with two mechanical loading conditions. Defects received morselized autograft prepared by mincing the excised cortical biopsy in sterile phosphate-buffered saline (PBS) [Autograft] contained within an electrospun, perforated poly-(ε-caprolactone) (PCL) nanofiber mesh tube. Limbs were stabilized with stiff [Stiff] or axially compliant [Compliant] fixation plates initially implanted in a locked configuration to prevent loading ($k_{axial} = 250 \pm 35$ N/mm), but after 4 weeks, the plates were surgically unlocked to enable load transfer

(k_{axial} = 8.0 ± 3.5 N/mm) (n = 6 to 8 per group) (*43*–*45*). For the second initial study, the experimental design featured three treatment groups with one mechanical loading condition. Defects received (i) mesenchymal condensations composed of three microparticle-containing hMSC sheets for a total of 6.0 × 10^6 cells with BMP-2–loaded MCM (1.9 μg) and unloaded GM [BMP-2 (hMSCs)], (ii) BMP-2 (1.9 μg) soaked onto 8-mm precut absorbable collagen sponge (INFUSE Bone Graft, Medtronic, Memphis, TN) 15 min before implantation [BMP-2 (collagen)], or (iii) morselized autograft in sterile PBS [Autograft], each contained within an electrospun, perforated PCL nanofiber mesh tube. Limbs were stabilized with stiff fixation plates [Stiff] that limit load transfer (k_{axial} = 260 ± 28 N/mm) (n = 7 to 10 per group), modified from prior studies (*43*–*45*).

Main study

The experimental design featured three treatment groups with two mechanical loading conditions (Table 1). Defects received mesenchymal condensations composed of three microparticle-containing hMSC sheets for a total of 6.0 × 10^6 cells incorporated with (i) unloaded MCM and GM [Empty/Control], (ii) BMP-2–loaded MCM (1.9 μg) and unloaded GM [BMP-2], or (iii) BMP-2–loaded MCM (1.9 μg) and TGF-β1–loaded GM (1.8 μg) [BMP-2 + TGF-β1] contained within an electrospun, perforated PCL nanofiber mesh tube. Limbs were stabilized with stiff [Stiff] or axially compliant [Compliant] fixation plates initially implanted in a locked configuration to prevent loading (k_{axial} = 250 ± 35 N/mm), but after 4 weeks, the plates were surgically unlocked to enable load transfer (k_{axial} = 8.0 ± 3.5 N/mm) (n = 3 to 10 per group) (*43*–*45*).

hMSC isolation and expansion

Bone marrow–derived hMSCs were derived from the posterior iliac crest of two healthy male donors (26 and 41 years of age) using a protocol approved by the University Hospitals of Cleveland Institutional Review Board. Cells were isolated using a Percoll gradient (Sigma-Aldrich, St. Louis, MO) and cultured in low-glucose Dulbecco's modified Eagle's medium (DMEM; Sigma-Aldrich, St. Louis, MO) containing 10% fetal bovine serum (Sigma-Aldrich), 1% penicillin/streptomycin (P/S; Thermo Fisher Scientific), and fibroblast growth factor–2 (10 ng/ml; R&D Systems, Minneapolis, MN) (*39*, *41*, *48*, *58*).

Hydroxyapatite microparticle mineral coating and BMP-2 loading

MCM were provided by W. L. Murphy (University of Wisconsin, Madison, WI). Their preparation using low carbonate (4.2 mM $NaHCO_3$) coating buffer and detailed characterization has been reported previously (*41*). Lyophilized MCM from the same batch as used in these prior studies, and our own (*48*), were loaded with a solution (100 μg/ml) of rhBMP-2 (W. Sebald, Department of Developmental Biology, University of Würzburg, Germany) in PBS for 4 hours at 37°C. BMP-2–loaded MCM were then centrifuged at 800*g* for 2 min and washed two times with PBS. Unloaded MCM without growth factor were incubated with PBS only and treated similarly.

GM synthesis and TGF-β1 loading

GM (*41*, *48*, *59*, *60*) were synthesized from 11.1% (w/v) gelatin type A (Sigma-Aldrich) using a water-in-oil single emulsion technique and cross-linked for 4 hours with 1% (w/v) genipin (Wako USA, Richmond, VA) (*60*). Hydrated GM were light blue in color and spherical in shape with an average diameter of 52.9 ± 40.2 μm and a cross-linking density of 25.5 ± 7.0% (*48*). Growth factor–loaded microspheres were prepared by soaking cross-linked, ultraviolet (UV)–sterilized GM in a solution (80 μg/ml) of rhTGF-β1 (PeproTech, Rocky Hill, NJ) in PBS for 2 hours at 37°C. Unloaded microspheres without growth factor were hydrated similarly using only PBS.

Nanofiber mesh production

Nanofiber meshes were formed by dissolving 12% (w/v) PCL (Sigma-Aldrich) in 90/10 (v/v) hexafluoro-2-propanol/dimethylformamide (Sigma-Aldrich). The solution was electrospun at a rate of 0.75 ml/hour onto a static aluminum collector. Sheets (9 mm by 20 mm) were cut from the product, perforated with a 1-mm biopsy punch (VWR, Radnor, PA), and glued into tubes around a 4.5-mm mandrel with UV glue (Dymax, Torrington, CT). Perforated PCL nanofiber mesh tubes were sterilized by 100% ethanol evaporation under UV light overnight and washed three times with sterile PBS before use.

Preparation of microparticle-incorporated mesenchymal condensations

Expanded hMSCs (2.0 × 10^6 cells per construct; passage 4) were thoroughly mixed with BMP-2–loaded MCM (1.6 μg/mg; 0.4 mg per construct) and TGF-β1–loaded GM (0.4 μg/mg; 1.5 mg per construct) in chemically defined medium [DMEM-HG (Sigma-Aldrich), 1% ITS+ Premix (Corning), 1 mM sodium pyruvate (HyClone), 100 μM nonessential amino acids (Lonza), 100 nM dexamethasone (MP Biomedicals, Solon, OH), 0.13 mM L-ascorbic acid-2-phosphate (Wako USA), and 1% P/S (Thermo Fisher Scientific)] (*27*, *39*). Five hundred microliters of the suspension was seeded onto the prewetted membrane of transwell inserts (3-μm pore size and 12 mm in diameter; Corning) and allowed to self-assemble into hMSC sheets for 2 days. After 24 hours, medium in the lower compartment was replaced. Control constructs containing either unloaded MCM and/or GM were prepared and cultured in a similar fashion. After 48 hours, three microparticle-incorporated hMSC sheets per group were combined into a sterile perforated PCL mesh tube to form the mesenchymal condensations for implantation.

Surgical procedure

Critical-sized (8 mm) bilateral segmental defects were created in the femora of 12-week-old male RNU rats (Taconic Biosciences Inc., Hudson, NY) under isoflurane anesthesia (*61*). Limbs were stabilized by custom internal fixation plates that allow controlled transfer of ambulatory loads in vivo (*43*) and secured to the femur by four bicortical miniature screws (J.I. Morris Co., Southbridge, MA). Animals were given subcutaneous injections of buprenorphine (0.04 mg/kg) every 8 hours for the first 48 hours postoperatively and 0.013 mg/kg every 8 hours for the following 24 hours, with or without carprofen (4 to 5 mg/kg) every 24 hours for 72 hours. In addition, 5 ml of 0.9% NaCl was administered subcutaneously to aid in recovery. All procedures were performed in strict accordance with the National Institutes of Health (NIH) Guide for the Care and Use of Laboratory Animals and the policies of the Institutional Animal Care and Use Committee at Case Western Reserve University (protocol no. 2015-0081) and the University of Notre Dame (protocol no. 14-05-1778).

In vivo x-ray and microCT

In vivo x-rays were obtained using an Xtreme scanner (Bruker, Billerica, MA) at 45 kilovolt peak (kVp), 0.4 mA, and 2-s exposure time. A

binary bridging score was assigned by two independent, blinded observers and determined as mineralized tissue fully traversing the defect. In vivo microCT scans were performed at 4, 8, and 12 weeks to assess longitudinal defect healing. For initial studies, animals were scanned using an Inveon microPET/CT system (Siemens Medical Solutions, Malvern, PA) at 45 kVp, 0.2 mA, and 35-μm isotropic voxels. Data were reconstructed using system default parameters for analyzing bone and accounting for the metal in the fixation plates. DICOM-exported files were processed for three-dimensional (3D) analysis (CTAn software, SKYSCAN/Bruker) using a gauss filter at 1.0 pixel radius and a global threshold range of 28 to 255 for all samples. Bone volume was determined in a standard region of interest (ROI) spanning the length of the defect. For the main study, animals were scanned using an Albira PET/SPECT/CT system (Bruker) at 45 kVp, 0.4 mA, and 125-μm voxel size. A global threshold was applied for each dataset, and bone volume was determined in a standard ROI spanning the length of the defect.

Ex vivo microCT

After 12 weeks, the animals were euthanized by CO_2 asphyxiation, and hind limbs were excised for high-resolution microCT analysis. Data were acquired using a SKYSCAN 1172 microCT scanner (Bruker) with a 0.5-mm aluminum filter at 75 kVp and 0.1 mA. Femora wrapped in gauze were placed in a plastic sample holder with the long axis oriented parallel to the image plane and scanned in PBS at 20-μm isotropic voxels, 560-ms integration time, rotation step of 0.5°, and frame averaging of 5. All samples were scanned within the same container using the same scanning parameters. All scans were then reconstructed using NRecon software (SKYSCAN/Bruker) with the same reconstruction parameters (ring artifact reduction of 5 and beam hardening correction of 20%). For 3D analysis (CTAn software, SKYSCAN/Bruker), a gauss filter at 1.0 pixel radius and a global threshold range of 65 to 255 was used. This segmentation approach allowed viewing of the normal bone architecture in the binary images as seen in the original reconstructed images (*62*). Three hundred twenty-five slices in the center of each defect were analyzed in a standard ROI using a 10-mm-diameter (total) or 5-mm-diameter (defect) circle centered on the medullary canal. Bone volume, bone volume fraction, pMOI, and the morphometric parameters—trabecular number, trabecular thickness, trabecular separation, structure model index, degree of anisotropy, and connectivity density—were calculated. Trabecular morphometry and pMOI of three age-matched femora were analyzed in the same manner for comparison. Proximal and distal total bone volume was calculated by halving the slice number in each sample and separately segmenting each half for comparison. All representative images were chosen on the basis of average bone volume values.

Biomechanical testing

Femora excised at 12 weeks were biomechanically tested in torsion to failure. Limbs were cleaned of soft tissue, and fixation plates were carefully removed. Bone ends were potted in Wood's metal (Alfa Aesar, Thermo Fisher Scientific), mounted on a Mark-10 TSTM-DC test stand with an MR50-12 torque sensor (1.35 N-m) and a 7i torque indicator (Mark-10 Corp., Copiague, NY) using custom fixtures and tested to failure at a rate of 3°/s. For each sample, maximum torque at failure was recorded, and torsional stiffness was computed as the slope of the linear region in the torque-rotation curve. Samples were compared to three age-matched, unoperated femurs.

Histological analysis

Day 2 hMSC sheets (n = 3 per group) were fixed in 10% neutral-buffered formalin (NBF) for 24 hours at 4°C before switching to 70% ethanol. One representative femur per group was taken for histology at weeks 4 and 12 after surgery and chosen on the basis of microCT-calculated average bone volumes. Femora were fixed in 10% NBF for 72 hours at 4°C and then transferred to 0.25 M EDTA (pH 7.4) for 14 days at 4°C under mild agitation on a rocker plate, with changes of the decalcification solution every 3 to 4 days. Following paraffin processing, 5-μm mid-sagittal sections were cut using a microtome (Leica Microsystems Inc., Buffalo Grove, IL) and stained with hematoxylin and eosin and Safranin-O/Fast-green. Light microscopy images were captured using an Olympus BX61VS microscope (Olympus, Center Valley, PA) with a Pike F-505 camera (Allied Vision Technologies, Stadtroda, Germany).

Quantitative reverse transcription polymerase chain reaction analysis

Day 2 hMSC sheets (n = 3 per group) were homogenized in TRI Reagent (Sigma-Aldrich) for subsequent total RNA extraction and complementary DNA (cDNA) synthesis (iScript Kit, Bio-Rad, Hercules, CA). One hundred nanograms of cDNA was amplified in duplicates in each 40-cycle reaction using a Mastercycler (Eppendorf, Hauppauge, NY) with annealing temperature set at 60°C, SYBR Premix Ex Taq II (Takara Bio Inc., Kusatsu, Shiga, Japan) and custom-designed quantitative reverse transcription polymerase chain reaction (qRT-PCR) primers (Life Technologies, Grand Island, NY; table S1). Transcript levels were normalized to glyceraldehyde-3-phosphate dehydrogenase, and gene expression was calculated as fold change using the comparative C_T method (*63*).

Immunoblotting

Day 2 hMSC sheets (n = 3 per group) were homogenized in CelLytic MT lysis buffer (Sigma-Aldrich) supplemented with Halt protease and phosphatase inhibitor cocktail (Thermo Fisher Scientific). Equal amounts (15 μg) of protein lysates, determined by a standard bicinchoninic acid (BCA) protein assay kit (Pierce, Thermo Fisher Scientific), were subjected to SDS–polyacrylamide gel electrophoresis using 10% NuPAGE Bis-Tris gels (Invitrogen, Thermo Fisher Scientific) and transferred to 0.45-μm polyvinylidene difluoride membranes (Millipore, Billerica, MA). Membranes were blocked with 5% bovine serum albumin in standard Tris-buffered saline, 0.1% Tween 20. The phosphorylation of intracellular SMAD3 and SMAD5 was detected using specific primary antibodies [anti–phospho-SMAD3 (ab52903) and anti–phospho-SMAD5 (ab92698), Abcam, Cambridge, MA], followed by horseradish peroxidase (HRP)–conjugated secondary antibodies (Jackson ImmunoResearch, West Grove, PA). Subsequently, the blots were stripped (Western Blot Stripping Buffer, Pierce, Thermo Fisher Scientific) and reprobed for the detection of the respective total protein [anti-SMAD3 (ab40854) and anti-SMAD5 (ab40771), Abcam] and loading control [anti–β-actin (A1978), Sigma-Aldrich] with respective HRP-conjugated secondary antibodies (Jackson ImmunoResearch). Bound antibodies were visualized with the enhanced chemiluminescence detection system (Pierce, Thermo Fisher Scientific) on autoradiography film (Thermo Fisher Scientific). The intensity of immunoreactive bands was quantified using ImageJ software (NIH, Bethesda, MD).

Statistical analysis

Differences in bone volume and bone volume accumulation rate by in vivo microCT at weeks 4, 8, and 12 were determined by two-way analysis of variance (ANOVA) with Tukey's post hoc test. Defect bridging was determined by χ^2 test for trend in each group; comparisons between groups were assessed with individual χ^2 tests and Bonferroni correction for multiple comparisons. Ex vivo microCT bone volume, bone volume fraction, and 3D morphometry were assessed by one- or two-way ANOVA with interaction and Tukey's post hoc test. Biomechanical properties were analyzed by two-way ANOVA with interaction and Tukey's post hoc test. Mechanical property regressions were performed using an exhaustive best subset algorithm to determine the best predictors of maximum torque and torsional stiffness from a subset of morphologic parameters measured, including minimum or mean pMOI (J_{min} or J_{mean}), bone volume fraction, binary bridging score (yes or no), trabecular thickness, trabecular separation, trabecular number, degree of anisotropy, and connectivity density based on AIC (*51*). The lowest AIC selects the best model while giving preference to models with less parameters. Last, the overall best model for each predicted mechanical property was compared to its measured value using type II general linear regression. All data are shown as means ± SD, some with individual data points or as box plots showing median as horizontal line, mean as "+," and 25th and 75th percentiles as boxes with whiskers at minimum and maximum values, respectively. Fold changes in mRNA expression and ratios of phosphorylated SMADs/total SMADs were analyzed by one-way ANOVA with Tukey's multiple comparison post hoc test. The significance level was set at $P < 0.05$ or lower. Groups with shared letters have no significant differences. GraphPad Prism software v6.0 (GraphPad Software, La Jolla, CA) was used for all analyses.

SUPPLEMENTARY MATERIALS

Supplementary material for this article is available at http://advances.sciencemag.org/cgi/content/full/5/8/eaax2476/DC1

Fig. S1. Effects of BMP-2–primed engineered mesenchymal condensations and routine clinical therapies on new bone quantity and architecture in the absence of mechanical cues.
Fig. S2. Effects of morselized autografts and in vivo mechanical loading on longitudinal bone formation and bone accumulation rate.
Fig. S3. Effects of morphogen priming of engineered mesenchymal condensations and in vivo mechanical loading on defect bridging.
Fig. S4. Effects of morphogen priming of engineered mesenchymal condensations and in vivo mechanical loading on new bone distribution and architecture.
Fig. S5. Best subset analysis of mechanical testing data.
Fig. S6. Effects of morphogen priming of engineered mesenchymal condensations on in vitro chondrogenic lineage specification at the time of implantation.
Fig. S7. Effects of morphogen priming of engineered mesenchymal condensations and in vivo mechanical loading on tissue-level bone regeneration at 4 weeks.
Fig. S8. Effects of morphogen priming of engineered mesenchymal condensations and in vivo mechanical loading on tissue-level bone regeneration at 12 weeks.
Table S1. Oligonucleotide primer sequences for qRT-PCR.

REFERENCES AND NOTES

1. V. Lefebvre, P. Bhattaram, Vertebrate skeletogenesis. *Curr. Top. Dev. Biol.* **90**, 291–317 (2010).
2. H. P. Gerber, T. H. Vu, A. M. Ryan, J. Kowalski, Z. Werb, N. Ferrara, VEGF couples hypertrophic cartilage remodeling, ossification and angiogenesis during endochondral bone formation. *Nat. Med.* **5**, 623–628 (1999).
3. A. Hosseini, D. A. Hogg, The effects of paralysis on skeletal development in the chick embryo. I. General effects. *J. Anat.* **177**, 159–168 (1991).
4. S. W. Verbruggen, B. Kainz, S. C. Shelmerdine, J. V. Hajnal, M. A. Rutherford, O. J. Arthurs, A. T. M. Phillips, N. C. Nowlan, Stresses and strains on the human fetal skeleton during development. *J. R. Soc. Interface* **15**, 20170593 (2018).
5. D. R. Carter, M. C. Van Der Meulen, G. S. Beaupré, Mechanical factors in bone growth and development. *Bone* **18**, 5S–10S (1996).
6. L. E. Claes, C. A. Heigele, C. Neidlinger-Wilke, D. Kaspar, W. Seidl, K. J. Margevicius, P. Augat, Effects of mechanical factors on the fracture healing process. *Clin. Orthop. Relat. Res.* **1998**, S132–S147 (1998).
7. A. E. Goodship, J. L. Cunningham, J. Kenwright, Strain rate and timing of stimulation in mechanical modulation of fracture healing. *Clin. Orthop. Relat. Res.* **1998**, S105–S115 (1998).
8. A. E. Goodship, J. Kenwright, The influence of induced micromovement upon the healing of experimental tibial fractures. *J. Bone Joint Surg.* **67**, 650–655 (1985).
9. J. Kenwright, J. B. Richardson, A. E. Goodship, M. Evans, D. J. Kelly, A. J. Spriggins, J. H. Newman, S. J. Burrough, J. D. Harris, D. I. Rowley, Effect of controlled axial micromovement on healing of tibial fractures. *Lancet* **2**, 1185–1187 (1986).
10. V. Röntgen, R. Blakytny, R. Matthys, M. Landauer, T. Wehner, M. Göckelmann, P. Jermendy, M. Amling, T. Schinke, L. Claes, A. Ignatius, Fracture healing in mice under controlled rigid and flexible conditions using an adjustable external fixator. *J. Orthop. Res.* **28**, 1456–1462 (2010).
11. S. Wolf, A. Janousek, J. Pfeil, W. Veith, F. Haas, G. Duda, L. Claes, The effects of external mechanical stimulation on the healing of diaphyseal osteotomies fixed by flexible external fixation. *Clin. Biomech.* **13**, 359–364 (1998).
12. R. Marsell, T. A. Einhorn, The biology of fracture healing. *Injury* **42**, 551–555 (2011).
13. L. C. Gerstenfeld, D. M. Cullinane, G. L. Barnes, D. T. Graves, T. A. Einhorn, Fracture healing as a post-natal developmental process: Molecular, spatial, and temporal aspects of its regulation. *J. Cell. Biochem.* **88**, 873–884 (2003).
14. P. M. Mountziaris, A. G. Mikos, Modulation of the inflammatory response for enhanced bone tissue regeneration. *Tissue Eng. Part B Rev.* **14**, 179–186 (2008).
15. L. Claes, S. Recknagel, A. Ignatius, Fracture healing under healthy and inflammatory conditions. *Nat. Rev. Rheumatol.* **8**, 133–143 (2012).
16. P. V. Giannoudis, H. Dinopoulos, E. Tsiridis, Bone substitutes: An update. *Injury* **36** (suppl. 3), S20–S27 (2005).
17. A. W. James, G. LaChaud, J. Shen, G. Asatrian, V. Nguyen, X. Zhang, K. Ting, C. Soo, A review of the clinical side effects of bone morphogenetic protein-2. *Tissue Eng. Part B Rev.* **22**, 284–297 (2016).
18. G. J. Meijer, J. D. de Bruijn, R. Koole, C. A. van Blitterswijk, Cell-based bone tissue engineering. *PLOS Med.* **4**, e9 (2007).
19. R. Dimitriou, E. Jones, D. McGonagle, P. V. Giannoudis, Bone regeneration: Current concepts and future directions. *BMC Med.* **9**, 66 (2011).
20. Y. Watanabe, N. Harada, K. Sato, S. Abe, K. Yamanaka, T. Matushita, Stem cell therapy: Is there a future for reconstruction of large bone defects? *Injury* **S47** (suppl. 1), S47–S51 (2016).
21. E. Farrell, O. P. van der Jagt, W. Koevoet, N. Kops, C. J. van Manen, C. A. Hellingman, H. Jahr, F. J. O'Brien, J. A. Verhaar, H. Weinans, G. J. van Osch, Chondrogenic priming of human bone marrow stromal cells: A better route to bone repair? *Tissue Eng. Part C Methods* **15**, 285–295 (2009).
22. A. M. McDermott, D. E. Mason, A. S. P. Lin, R. E. Guldberg, J. D. Boerckel, Influence of structural load-bearing scaffolds on mechanical load- and BMP-2-mediated bone regeneration. *J. Mech. Behav. Biomed. Mater.* **62**, 169–181 (2016).
23. D. E. Ingber, V. C. Mow, D. Butler, L. Niklason, J. Huard, J. Mao, I. Yannas, D. Kaplan, G. Vunjak-Novakovic, Tissue engineering and developmental biology: Going biomimetic. *Tissue Eng.* **12**, 3265–3283 (2006).
24. E. Alsberg, K. W. Anderson, A. Albeiruti, J. A. Rowley, D. J. Mooney, Engineering growing tissues. *Proc. Natl. Acad. Sci. U.S.A.* **99**, 12025–12030 (2002).
25. F. E. Freeman, A. B. Allen, H. Y. Stevens, R. E. Guldberg, L. M. McNamara, Effects of in vitro endochondral priming and pre-vascularisation of human MSC cellular aggregates in vivo. *Stem Cell Res. Ther.* **6**, 218 (2015).
26. C. Scotti, B. Tonnarelli, A. Papadimitropoulos, A. Scherberich, S. Schaeren, A. Schauerte, J. Lopez-Rios, R. Zeller, A. Barbero, I. Martin, Recapitulation of endochondral bone formation using human adult mesenchymal stem cells as a paradigm for developmental engineering. *Proc. Natl. Acad. Sci. U.S.A.* **107**, 7251–7256 (2010).
27. P. N. Dang, S. Herberg, D. Varghai, H. Riazi, D. Varghai, A. McMillan, A. Awadallah, L. M. Phillips, O. Jeon, M. K. Nguyen, N. Dwivedi, X. Yu, W. L. Murphy, E. Alsberg, Endochondral ossification in critical-sized bone defects via readily implantable scaffold-free stem cell constructs. *Stem Cells Transl. Med.* **6**, 1644–1659 (2017).
28. N. Harada, Y. Watanabe, K. Sato, S. Abe, K. Yamanaka, Y. Sakai, T. Kaneko, T. Matsushita, Bone regeneration in a massive rat femur defect through endochondral ossification achieved with chondrogenically differentiated MSCs in a degradable scaffold. *Biomaterials* **35**, 7800–7810 (2014).
29. C. S. Bahney, D. P. Hu, A. J. Taylor, F. Ferro, H. M. Britz, B. Hallgrimsson, B. Johnstone, T. Miclau, R. S. Marcucio, Stem cell-derived endochondral cartilage stimulates bone healing by tissue transformation. *J. Bone Mine. Res.* **29**, 1269–1282 (2014).
30. R. Tuli, S. Tuli, S. Nandi, X. Huang, P. A. Manner, W. J. Hozack, K. G. Danielson, D. J. Hall, R. S. Tuan, Transforming growth factor-β-mediated chondrogenesis of human mesenchymal progenitor cells involves N-cadherin and mitogen-activated protein kinase and Wnt signaling cross-talk. *J. Biol. Chem.* **278**, 41227–41236 (2003).

31. B. S. Yoon, D. A. Ovchinnikov, I. Yoshii, Y. Mishina, R. R. Behringer, K. M. Lyons, *Bmpr1a* and *Bmpr1b* have overlapping functions and are essential for chondrogenesis in vivo. *Proc. Natl. Acad. Sci. U.S.A.* **102**, 5062–5067 (2005).
32. V. Lefebvre, P. Smits, Transcriptional control of chondrocyte fate and differentiation. *Birth Defects Res. C Embryo Today* **75**, 200–212 (2005).
33. H. Akiyama, Control of chondrogenesis by the transcription factor Sox9. *Mod. Rheumatol.* **18**, 213–219 (2014).
34. K. Pelttari, A. Winter, E. Steck, K. Goetzke, T. Hennig, B. G. Ochs, T. Aigner, W. Richter, Premature induction of hypertrophy during in vitro chondrogenesis of human mesenchymal stem cells correlates with calcification and vascular invasion after ectopic transplantation in SCID mice. *Arthritis Rheum.* **54**, 3254–3266 (2006).
35. E. Farrell, S. K. Both, K. I. Odörfer, W. Koevoet, N. Kops, F. J. O'Brien, R. J. Baatenburg de Jong, J. A. Verhaar, V. Cuijpers, J. Jansen, R. G. Erben, G. J. van Osch, In-vivo generation of bone via endochondral ossification by in-vitro chondrogenic priming of adult human and rat mesenchymal stem cells. *BMC Musculoskelet. Disord.* **12**, 31 (2011).
36. E. J. Sheehy, T. Vinardell, C. T. Buckley, D. J. Kelly, Engineering osteochondral constructs through spatial regulation of endochondral ossification. *Acta Biomater.* **9**, 5484–5492 (2013).
37. W. Yang, S. K. Both, G. J. van Osch, Y. Wang, J. A. Jansen, F. Yang, Effects of in vitro chondrogenic priming time of bone-marrow-derived mesenchymal stromal cells on in vivo endochondral bone formation. *Acta Biomater.* **13**, 254–265 (2015).
38. C. Scotti, E. Piccinini, H. Takizawa, A. Todorov, P. Bourgine, A. Papadimitropoulos, A. Barbero, M. G. Manz, I. Martin, Engineering of a functional bone organ through endochondral ossification. *Proc. Natl. Acad. Sci. U.S.A.* **110**, 3997–4002 (2013).
39. L. D. Solorio, E. L. Vieregge, C. D. Dhami, P. N. Dang, E. Alsberg, Engineered cartilage via self-assembled hMSC sheets with incorporated biodegradable gelatin microspheres releasing transforming growth factor-β1. *J. Control Release* **158**, 224–232 (2012).
40. A. M. McDermott, S. Herberg, D. E. Mason, H. B. Pearson, J. H. Dawahare, J. M. Collins, M. W. Grinstaff, D. J. Kelly, E. Alsberg, J. D. Boerckel, Recapitulating bone development for tissue regeneration through engineered mesenchymal condensations and mechanical cues. *Sci. Transl. Med.* **11**, eaav7756 (2019).
41. P. N. Dang, N. Dwivedi, L. M. Phillips, X. Yu, S. Herberg, C. Bowerman, L. D. Solorio, W. L. Murphy, E. Alsberg, Controlled dual growth factor delivery from microparticles incorporated within human bone marrow-derived mesenchymal stem cell aggregates for enhanced bone tissue engineering via endochondral ossification. *Stem Cells Transl. Med.* **5**, 206–217 (2016).
42. P. N. Dang, N. Dwivedi, X. Yu, L. M. Phillips, C. Bowerman, W. L. Murphy, E. Alsberg, Guiding chondrogenesis and osteogenesis with mineral-coated hydroxyapatite and BMP-2 incorporated within high-density hMSC aggregates for bone regeneration. *ACS Biomater. Sci. Eng.* **2**, 30–42 (2016).
43. J. D. Boerckel, K. M. Dupont, Y. M. Kolambkar, A. S. Lin, R. E. Guldberg, In vivo model for evaluating the effects of mechanical stimulation on tissue-engineered bone repair. *J. Biomech. Eng.* **131**, 084502 (2009).
44. J. D. Boerckel, Y. M. Kolambkar, H. Y. Stevens, A. S. Lin, K. M. Dupont, R. E. Guldberg, Effects of in vivo mechanical loading on large bone defect regeneration. *J. Orthop. Res.* **30**, 1067–1075 (2012).
45. J. D. Boerckel, B. A. Uhrig, N. J. Willett, N. Huebsch, R. E. Guldberg, Mechanical regulation of vascular growth and tissue regeneration in vivo. *Proc. Natl. Acad. Sci. U.S.A.* **108**, E674–E680 (2011).
46. V. Glatt, N. Bartnikowski, N. Quirk, M. Schuetz, C. Evans, Reverse dynamization: Influence of fixator stiffness on the mode and efficiency of large-bone-defect healing at different doses of rhBMP-2. *J. Bone Joint Surg.* **98**, 677–687 (2016).
47. V. Glatt, M. Miller, A. Ivkovic, F. Liu, N. Parry, D. Griffin, M. Vrahas, C. Evans, Improved healing of large segmental defects in the rat femur by reverse dynamization in the presence of bone morphogenetic protein-2. *J. Bone J. Surg.* **94**, 2063–2073 (2012).
48. S. Herberg, D. Varghai, Y. Cheng, A. D. Dikina, P. N. Dang, M. W. Rolle, E. Alsberg, High-density human mesenchymal stem cell rings with spatiotemporally-controlled morphogen presentation as building blocks for engineering bone diaphyseal tissue. *Nanotheranostics* **2**, 128–143 (2018).
49. X. Yu, A. Khalil, P. N. Dang, E. Alsberg, W. L. Murphy, Multilayered inorganic microparticles for tunable dual growth factor delivery. *Adv. Funct. Mater.* **24**, 3082–3093 (2014).
50. C. D. Kegelman, D. E. Mason, J. H. Dawahare, D. J. Horan, G. D. Vigil, S. S. Howard, A. G. Robling, T. M. Bellido, J. D. Boerckel, Skeletal cell YAP and TAZ combinatorially promote bone development. *FASEB J.* **32**, 2706–2721 (2018).
51. H. Akaike, A new look at the statistical model identification. *IEEE Trans. Autom. Control* **19**, 716–723 (1974).
52. J. Massagué, TGF-β signal transduction. *Annu. Rev. Biochem.* **67**, 753–791 (1998).
53. K. Karamboulas, H. J. Dranse, T. M. Underhill, Regulation of BMP-dependent chondrogenesis in early limb mesenchyme by TGF signals. *J. Cell Sci.* **123**, 2068–2076 (2010).
54. J. van der Stok, M. K. Koolen, H. Jahr, N. Kops, J. H. Waarsing, H. Weinans, O. P. van der Jagt, Chondrogenically differentiated mesenchymal stromal cell pellets stimulate endochondral bone regeneration in critical-sized bone defects. *Eur. Cell. Mater.* **27**, 137–148 (2014).
55. L. E. Claes, C. A. Heigele, Magnitudes of local stress and strain along bony surfaces predict the course and type of fracture healing. *J. Biomech.* **32**, 255–266 (1999).
56. J. D. Boerckel, Y. M. Kolambkar, K. M. Dupont, B. A. Uhrig, E. A. Phelps, H. Y. Stevens, A. J. Garcia, R. E. Guldberg, Effects of protein dose and delivery system on BMP-mediated bone regeneration. *Biomaterials* **32**, 5241–5251 (2011).
57. F. Faul, E. Erdfelder, A. Buchner, A. G. Lang, Statistical power analyses using G*Power 3.1: Tests for correlation and regression analyses. *Behav. Res. Methods* **41**, 1149–1160 (2009).
58. L. D. Solorio, C. D. Dhami, P. N. Dang, E. L. Vieregge, E. Alsberg, Spatiotemporal regulation of chondrogenic differentiation with controlled delivery of transforming growth factor-β1 from gelatin microspheres in mesenchymal stem cell aggregates. *Stem Cells Transl. Med.* **1**, 632–639 (2012).
59. P. N. Dang, L. D. Solorio, E. Alsberg, Driving cartilage formation in high-density human adipose-derived stem cell aggregate and sheet constructs without exogenous growth factor delivery. *Tissue Eng. Part A* **20**, 3163–3175 (2014).
60. L. D. Solorio, A. S. Fu, R. Hernández-Irizarry, E. Alsberg, Chondrogenic differentiation of human mesenchymal stem cell aggregates via controlled release of TGF-β1 from incorporated polymer microspheres. *J. Biomed. Mater. Res. A* **92**, 1139–1144 (2010).
61. M. E. Oest, K. M. Dupont, H. J. Kong, D. J. Mooney, R. E. Guldberg, Quantitative assessment of scaffold and growth factor-mediated repair of critically sized bone defects. *J. Orthop. Res.* **25**, 941–950 (2007).
62. M. L. Bouxsein, S. K. Boyd, B. A. Christiansen, R. E. Guldberg, K. J. Jepsen, R. Muller, Guidelines for assessment of bone microstructure in rodents using micro-computed tomography. *J. Bone Miner. Res.* **25**, 1468–1486 (2010).
63. T. D. Schmittgen, K. J. Livak, Analyzing real-time PCR data by the comparative C(T) method. *Nat. Protoc.* **3**, 1101–1108 (2008).

Acknowledgments: We thank the staff of the Freimann Life Science Center at the University of Notre Dame (ND) and the Animal Resource Center at Case Western Reserve University (CWRU) for animal care and husbandry. We also thank the staff of the ND Integrated Imaging Facility and the CWRU Imaging Research Core Facility for imaging support, E. M. Greenfield at the CWRU Orthopaedic Research Facilities for imaging and biomechanical testing support, and A. Awadallah at the CWRU Histology Core Facility for technical support. We also thank X. Yu and W. L. Murphy at the University of Wisconsin, Madison, WI for providing the MCM. **Funding:** We gratefully acknowledge funding from the NIH's National Institute of Dental and Craniofacial Research (F32DE024712 to S.H.), National Institute of Arthritis and Musculoskeletal and Skin Diseases (R01AR066193, R01AR063194, and R01AR069564 to E.A. and T32AR007505 to D.S.A.), National Heart, Lung, and Blood Institute (T32HL134622 to R.T.), National Institute of Biomedical Imaging and Bioengineering (R01EB023907 to E.A.), National Center for Advancing Translational Sciences (TL1 TR000441 to D.S.A.), the Ohio Biomedical Research Commercialization Program under award number TECG20150782 (to E.A.), the Naughton Foundation (to A.M.M. and J.D.B.), and the Indiana Clinical and Translational Sciences Institute, grant number UL1TR001108 from the NIH (to J.D.B.). The contents of this publication are solely the responsibility of the authors and do not necessarily represent the official views of the NIH. **Author contributions:** S.H., A.M.M., R.T., J.D.B., and E.A. designed the first initial in vivo study and analyzed the data. F.H., Y.B.L., J.H.D., Y.C., K.U., and P.C.W. assisted with the animal surgeries. S.H., P.N.D., J.D.B., and E.A. designed the second initial in vivo study and analyzed the data. D.S.A., J.H.D., D.V., H.P., J.-Y.S., A.M., and A.D.D. assisted with the animal surgeries. S.H., A.M.M., J.D.B., and E.A. designed the main study experiments, analyzed the data, and wrote the manuscript. All authors collected data and commented on and approved the final manuscript. J.D.B. and E.A. conceived and supervised the research. **Competing interests:** E.A. is an inventor on patents related to this work filed by CWRU (no. 16/044,182, filed 24 July 2018; no. 13/863,364, filed 19 April 2013, issued 24 July 2018; no. 15/258,666, filed 7 September 2016; no. 15/698,429, filed 7 September 2017; no. 62/655,136, filed 9 April 2019). The authors declare that they have no other competing interests. **Data and materials availability:** All data needed to evaluate the conclusions in the paper are present in the paper and/or the Supplementary Materials. Additional data related to this paper may be requested from the authors.

Submitted 6 March 2019
Accepted 19 July 2019
Published 28 August 2019
10.1126/sciadv.aax2476

Citation: S. Herberg, A. M. McDermott, P. N. Dang, D. S. Alt, R. Tang, J. H. Dawahare, D. Varghai, J.-Y. Shin, A. McMillan, A. D. Dikina, F. He, Y. B. Lee, Y. Cheng, K. Umemori, P. C. Wong, H. Park, J. D. Boerckel, E. Alsberg, Combinatorial morphogenetic and mechanical cues to mimic bone development for defect repair. *Sci. Adv.* **5**, eaax2476 (2019).

Science Advances

Combinatorial morphogenetic and mechanical cues to mimic bone development for defect repair

S. Herberg, A. M. McDermott, P. N. Dang, D. S. Alt, R. Tang, J. H. Dawahare, D. Varghai, J.-Y. Shin, A. McMillan, A. D. Dikina, F. He, Y. B. Lee, Y. Cheng, K. Umemori, P. C. Wong, H. Park, J. D. Boerckel and E. Alsberg

Sci Adv **5** (8), eaax2476.
DOI: 10.1126/sciadv.aax2476